True triaxial behavior of sandy soils under both drained and undrained conditions: A discrete element perspective

Seyedeh Fateme Faraji[1]   Wu Qixin[2]   Zheng Junjie[1]

([1] School of Civil and Hydraulic Engineering, Huazhong University of Science and Technology, Wuhan 430074, China)
([2] School of Civil Engineering, Wuhan University, Wuhan 430072, China)

Abstract: An advanced discrete element servomechanism that can simultaneously and independently control the evolution equations of six stress and strain components without introducing severe stress concentration is implemented. Such a comprehensive series of discrete element method simulations of both drained and undrained behavior of transversely isotropic sandy soils are successfully conducted in the true triaxial setting. During the simulation process, the evolution patterns of the load-bearing structure of the granular specimen are tracked using a contact-normal-based fabric tensor. The simulation results show that sandy soils exhibit more significant non-coaxiality between the loading direction and the major principal direction of the fabric tensor under extension than under compression. Therefore, the fabric of the sandy soils under extension has a stronger tendency to evolve toward the loading direction than that under compression, causing a more significant disturbance to the load-bearing structure. Consequently, compared with the extension loading condition, the transversely isotropic specimen under compression exhibits a higher shear strength and stronger dilatancy under drained conditions and a stronger liquefaction resistance under undrained conditions.

Key words: granular materials; true triaxial test; discrete element method; fabric evolution

DOI: 10.3969/j.issn.1003 − 7985.2024.04.002

G ranular materials, such as sand, exhibit complex mechanical behavior under external loading scenarios, especially when the influence of true triaxial loading conditions is considered[1].

A series of experimental and numerical studies have determined the intermediate principal stress ratio. The loading path in the true triaxial test can be determined using the dimensionless intermediate principal stress ratio $b = $

$(\sigma_2 - \sigma_3)/(\sigma_1 - \sigma_3)$.

The b value plays a crucial role in the mechanical characterics of sand under various conditions, including dilation[2–9], shear strength[10–16], formation of shear localization[17–18], and shape of the failure surface[11, 18]. In the meantime, the undrained behavior of granular materials is crucial in designing geotechnical structures. Under undrained conditions, granular soils undergo liquefaction failure with continuous accumulation of residual strain, which is significantly influenced by the intermediate principal stress ratio[19].

To gain a deeper understanding of the microscopic mechanism underlying the macroscale observations, the discrete element method (DEM) has been widely utilized to analyze the mechanical behavior of sand under true triaxial loading conditions. DEM simulations allow for a thorough understanding of the response of granular soils by considering the interplay between external loadings and internal fabric evolution[20]. For instance, Xie et al.[21] discussed three-dimensional (3D) DEM simulations of true triaxial tests and reported that the critical stress ratio is dependent on the intermediate principal stress ratio.

However, DEM simulations of true triaxial tests have scarcely been conducted under undrained conditions mainly because of the difficulty in performing the undrained tests, i.e., maintaining the specimen's volume constant while implementing the true triaxial loading condition. Using a more advanced but computationally more expansive coupled technique, Foroutan and Mirghasemi[22] developed a CFDEM solver that considers compressible fluid and moving meshes and is calibrated against the results of Nevada sand. Based on this technique, a series of simulations of undrained true triaxial tests were successfully conducted. Foroutan and Mirghasemi[23] further calculated the hydrodynamic forces on the particles and evaluated the ratio of the particle-fluid interaction force to the resultant force on the particles.

Moreover, various studies have explored the use of micromechanical data to create or adjust fabric evolution laws of micromechanics-based constitutive models. These studies[24–26] involve developing constitutive models based on stress-strain curves under both drained and undrained conditions, emphasizing the vital role of fabric evolution details in understanding the mechanical characteristics of

sand. As the fabric evolution data of granular materials under both drained and undrained triaxial loading conditions are limited, further studies are required.

This study first illustrates the creation of a polyhedral sample configuration utilizing the PFC3D version 5.0 software[27]. Then, a brief introduction of the simulation procedure and the advanced servomechanism that can apply true triaxial loading paths under both drained and undrained conditions is presented. To gain a better understanding of the mechanical properties of granular soils subjected to true triaxial loading, this research attempts to analyze the data derived from micromechanical evolution under both drained and undrained conditions, which can well explain the macroscale observations. As such, this research provides useful insights into the development of micromechanics-based constitutive models.

1 Simulation Procedures

The Particle Flow Code, developed by Itasca Consulting Group, Inc. [27], is used in this work. As Cundall[28] provided a detailed discussion of the principles of DEM, the specifics will not be repeated here. Clumped granular particles comprising two identical and overlapping spheres were created to depict the natural elongation of sandy particles. The aspect ratio of all of the elongated particles is set as 0.6, and the equivalent diameter (the diameter of a spherical particle with identical volume) of all of the clumped particles falls within the range of [0.13, 0.33] mm. The particle size distribution curve of the employed numerical specimen is a close approximation of the Toyoura sand, with $d_{50} \approx 0.23$ mm[8].

Cuboid specimens with the dimensions of 13 mm × 13 mm × 16.5 mm were first created using the under-compaction method[29], as shown in Fig. 1(a). Then, a polyhedron comprising 26 facets is generated within the cuboid specimen. The size of the polyhedral specimen is quantified through an inscribed sphere with a radius of 5 mm. As shown in Fig. 1(b), the particles outside the polyhedral specimen are deleted, and the remaining more than 6 000 particles are deemed the representative element volume.

After the specimens had been generated, they were gradually compacted to reach a minimum confining pressure of 10 kPa. The void ratio of the specimens before the true triaxial loading can be adjusted by altering the interparticle friction coefficient (μ). A μ value of 0.5 was utilized for the loose specimens, and μ values of 0.3 and 0.1 were used for the medium-dense and dense specimens, respectively. Subsequently, all specimens were consolidated gradually to a desired confining pressure (e.g., $p = 100$, 200, 500 kPa). Afterward, the interparticle friction coefficient was reset to 0.5 before the true
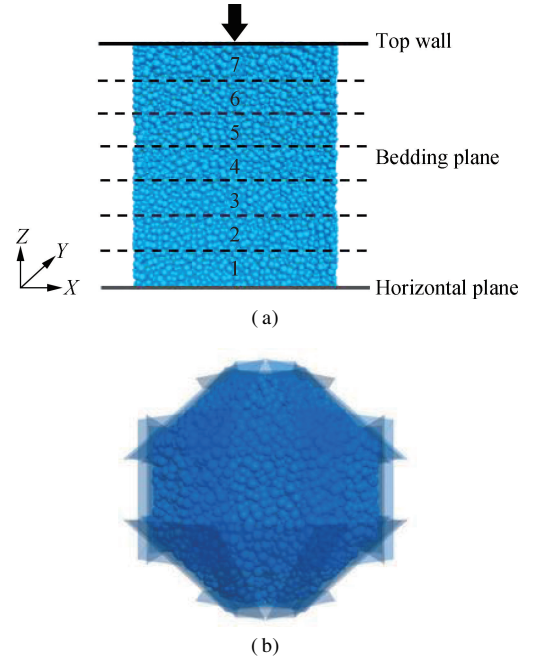

Fig. 1 Specimen preparation. (a) Transversely isotropic specimen; (b) Polyhedral specimen generation

triaxial loading experiments were conducted. Each particle has an identical normal and shear stiffness value of $k_n = k_s = 100$ kN/m and a solid density of $\rho = 2\,600$ kg/m³. A numerical dampening factor of $\xi = 0.3$ is used to reduce computational effort. To keep the loading process in quasi-static equilibrium, strain increments are only applied when the ratio of the maximum unbalanced force to the mean normal contact force is less than 0.001. Table 1 provides a detailed summary of all relevant parameters used in the simulations.

Table 1 Variables employed in three-dimensional (DEM) simulations

Parameter	Value
Particle solid density $\rho/(\mathrm{kg \cdot m^{-3}})$	2 600
Equivalent diameter of clump r/mm	0.13-0.33
Normal stiffness of particle $k_n/(\mathrm{kN \cdot m^{-1}})$	100
Tangential stiffness of particle $k_s/(\mathrm{kN \cdot m^{-1}})$	100
Frictional coefficient μ	0.5
Damping parameter ξ	0.3

The stress tensor σ'_{ij} and Biot strain ε_{ij} are calculated based on the boundary forces and movements in this analysis. The formulas for calculating σ'_{ij} and ε_{ij} are described in detail in the work of Li et al. [30]. In addition, the value of σ'_{ij} is used to calculate the average effective normal stress p' and the generalized deviatoric stress q in the following manner:

$$p' = \frac{\sigma'_{xx} + \sigma'_{yy} + \sigma'_{zz}}{3} \tag{1}$$

$$q = \frac{\sqrt{2}}{2}\sqrt{(\sigma'_{xx} - \sigma'_{yy})^2 + (\sigma'_{xx} - \sigma'_{zz})^2 + (\sigma'_{yy} - \sigma'_{zz})^2 + 6(\sigma^2_{xy} + \sigma^2_{xz} + \sigma^2_{yz})} \tag{2}$$

The Biot strain tensor[13] is a 3D symmetric second-order tensor. The volumetric strain is more accurately stated using the invariants of the tensor rather than utilizing the total of the principal strains. This is particularly important when dealing with finite and massive deformations, as it ensures higher accuracy. Consequently, the volumetric strain ε_v and generalized deviatoric strain ε_q can be determined as follows:

$$\varepsilon_v = 1 - \det(\delta_{ij} - \varepsilon_{ij}) \tag{3}$$

$$\varepsilon_q = \frac{\sqrt{2}}{3}\sqrt{(\varepsilon_{xx} - \varepsilon_{yy})^2 + (\varepsilon_{xx} - \varepsilon_{zz})^2 + (\varepsilon_{yy} - \varepsilon_{zz})^2 + 6(\varepsilon_{xy}^2 + \varepsilon_{xz}^2 + \varepsilon_{yz}^2)} \tag{4}$$

Notably, the employed servomechanism can independently and simultaneously control the evolution of six stress and strain components without introducing stress concentration and strain nonuniformity. Detailed information on the servomechanism has been provided in previous studies[31-32] and therefore omitted here for brevity. Table 2 summarizes all of the simulation conditions considered in this study. As shown in Table 2, a total of 54 simulation cases were conducted in this study. Notably, the initial fabric norm $F \geqslant 0$ quantifies the degree of the fabric anisotropy of the granular specimen. When $F = 0$, the specimen is isotropic. A higher magnitude of F indicates a higher degree of fabric anisotropy possessed by the specimen.

Table 2 Summary of simulated DEM drained and undrained loading tests

Test series	b	Density	p/kPa	F	e
I	0	Loose	100	0.423	0.712
			200	0.478	0.707
			500	0.479	0.684
		Medium dense	100	0.396	0.660
			200	0.389	0.670
			500	0.397	0.650
		Dense	100	0.250	0.579
			200	0.246	0.575
			500	0.243	0.559
II	0.5	Loose	100	0.423	0.712
			200	0.478	0.707
			500	0.479	0.684
		Medium dense	100	0.396	0.660
			200	0.389	0.670
			500	0.397	0.650
		Dense	100	0.250	0.579
			200	0.246	0.575
			500	0.243	0.559
III	1.0	Loose	100	0.423	0.712
			200	0.478	0.707
			500	0.479	0.684
		Medium dense	100	0.396	0.660
			200	0.389	0.670
			500	0.397	0.650
		Dense	100	0.250	0.579
			200	0.246	0.575
			500	0.243	0.559

Note: b is the intermediate principal stress ratio; e is the void ratio.

Taking the medium-dense specimens as an example, Figs. 2 and 3 show the measured intermediate principal stress ratio and the mean normal stress of the specimen under drained conditions, respectively. During the entire simulation process, both the mean principal normal stress p' and the intermediate principal stress ratio b are maintained constant for the specimens under drained loading conditions.
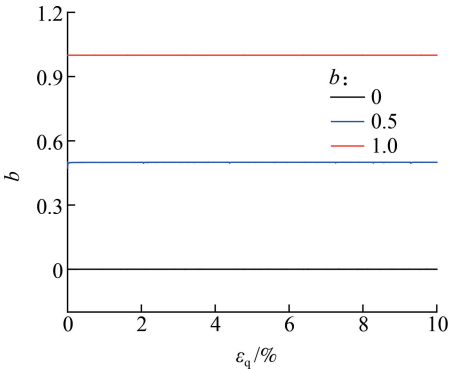

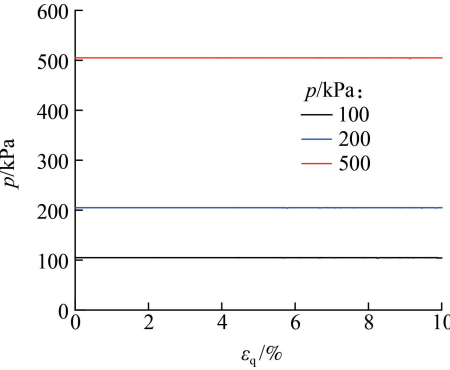**Fig. 2** Measured intermediate principal stress ratio

Fig. 3 Measured mean normal stress

Fig. 4 plots the volumetric strain of specimens subjected to undrained true triaxial loading conditions. Notably, the greatest ε_v is smaller than 9×10^{-6}, confirming the
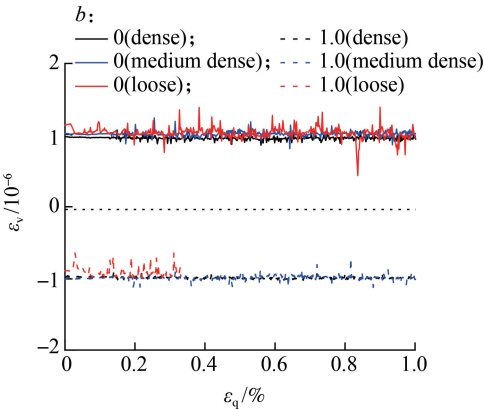

Fig. 4 Evolution of the volumetric strains ε_v under undrained conditions for specimens with various densities

validity of the servomechanism for maintaining a constant volume of the specimen.

2　Simulation Results

2.1　Macromechanical behavior

This section describes the macroscopic responses of granular materials under both drained and undrained loading conditions in the true triaxial shearing tests. Fig. 5
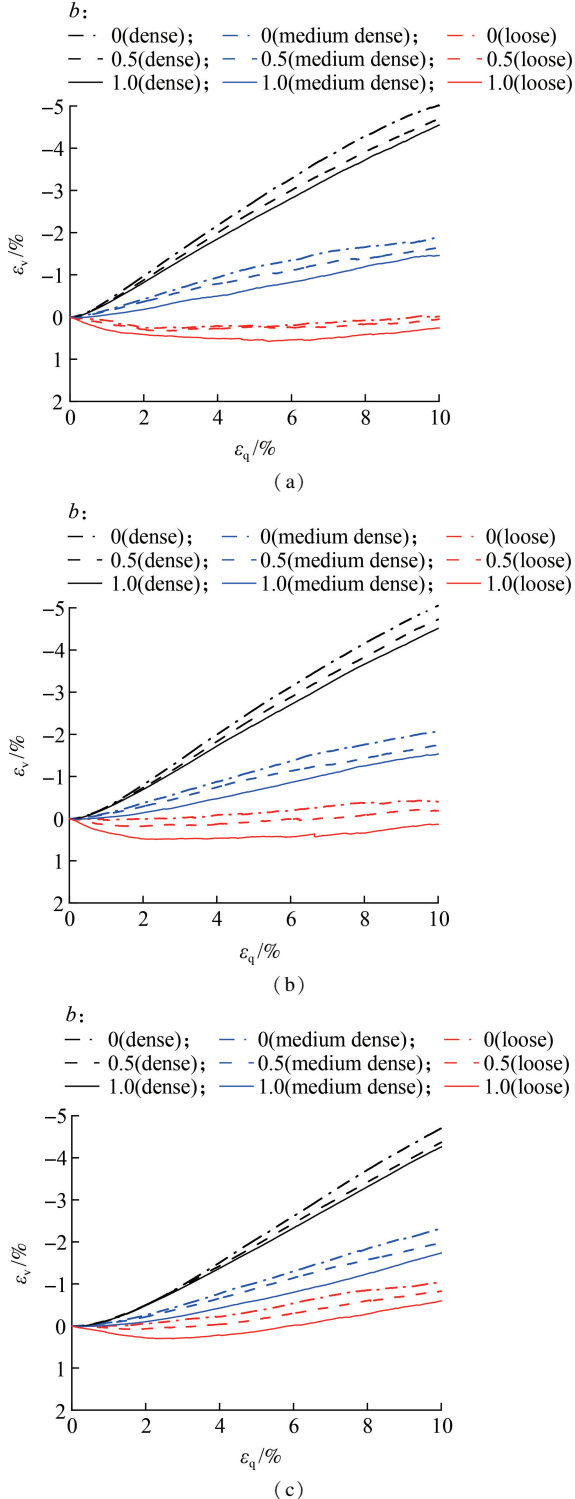

Fig. 5　ε_v vs. ε_q for specimens under drained conditions. (a) $p = 100$ kPa; (b) $p = 200$ kPa; (c) $p = 500$ kPa

illustrates the evolution of volumetric strain ε_v vs. deviatoric strain ε_q under drained true triaxial stress at different confining pressure levels with various loading paths.

As shown in Fig. 5(a), specimens with different densities respond differently to the applied loadings. Notably, all of the specimens exhibit more contractive behavior as the b value increases. Dense specimens first contract at low shear strain levels and then start to dilate, whereas loose specimens mainly exhibit contractive behavior under all loading conditions. As shown in Figs. 5 (b) and (c), similar observations can be obtained for the specimens under $p = 200$ and 500 kPa.

Considering the confining pressure, Fig. 6 shows the shear stress-strain characteristics of specimens with different densities (i.e., loose, medium dense, and dense) under both drained compression and extension. As shown in Fig. 6(a), both the maximum deviatoric stress and shear strain level of all of the specimens increase as the confining pressure increases from 100 to 500 kPa. Similarly, Figs. 6(b) and (c) show the loading conditions under $b = 0.5$ and 1.0, respectively. The comparison of Figs. 6(a), (b), and (c) shows that, under otherwise identical conditions, the specimens with higher b values tend to exhibit lower deviatoric stress q.

Taking the medium-dense specimens as an example, Fig. 7 shows the stress-strain curves of the specimens under undrained true triaxial loading conditions. Figs. 7 (a), (b), and (c) plot the shear stress-strain curves of the medium-dense samples with $b = 0$, 0.5, and 1.0, respectively. For the specimens with the same b value, the stress ratio q/p' tends to increase with the increase in confining pressure. Under the same confining pressure, the stress ratio decreases as the intermediate principal stress ratio increases.

Fig. 8 further plots the effective stress paths in the q/p' plane of specimens under the same loading conditions as that of Fig. 7. Notably, Fig. 8 shows that, under otherwise identical conditions, the dilative tendency of the specimen becomes stronger as the confining pressure increases or the b value decreases.

Fig. 9 summarizes the peak stress ratio q/p' for both dense and loose specimens, considering confining pressures and intermediate principal stress ratios under both drained and undrained conditions. As illustrated in Fig. 9 (a), the influence of confining pressure on the peak q/p' of the specimens under drained conditions is negligible, whereas the density of the specimens has significant effects. Fig. 9(b) summarizes the peak stress ratio of the specimens under undrained conditions. Notably, the confining pressure has a beneficial effect on the stress ratio under undrained conditions. Table 3 summarizes the peak stress ratios of the specimens under different loading conditions. Loose specimens under extension consistently exhibit the lowest values, particularly at lower confining
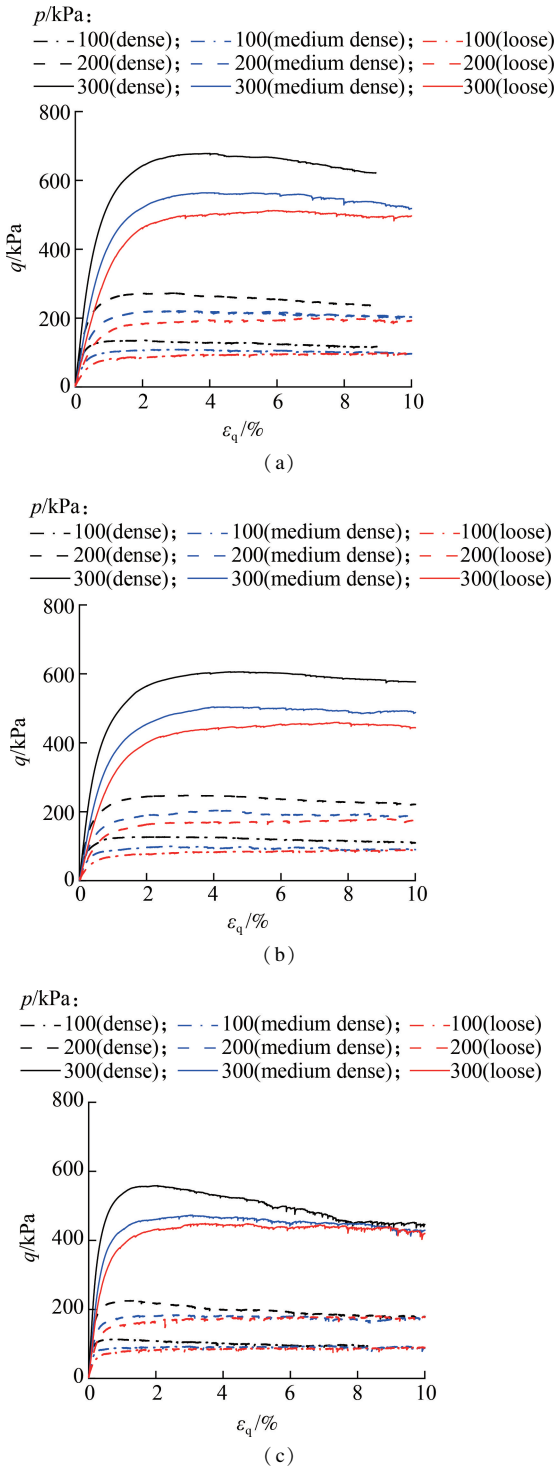
Fig. 6 q vs. ε_q for specimens under drained conditions. (a) $b = 0$; (b) $b = 0.5$; (c) $b = 1.0$

pressure $p = 100$ kPa.

2.2 Fabric evolutions

A better understanding of the fabric evolution characteristics is essential to comprehending granular material macromechanical behavior[33]. A deviatoric contact-normal-based fabric tensor $\boldsymbol{F}$ is used to quantify the load-bearing structure of granular materials, which can be useful in the construction of micromechanics-based consti-
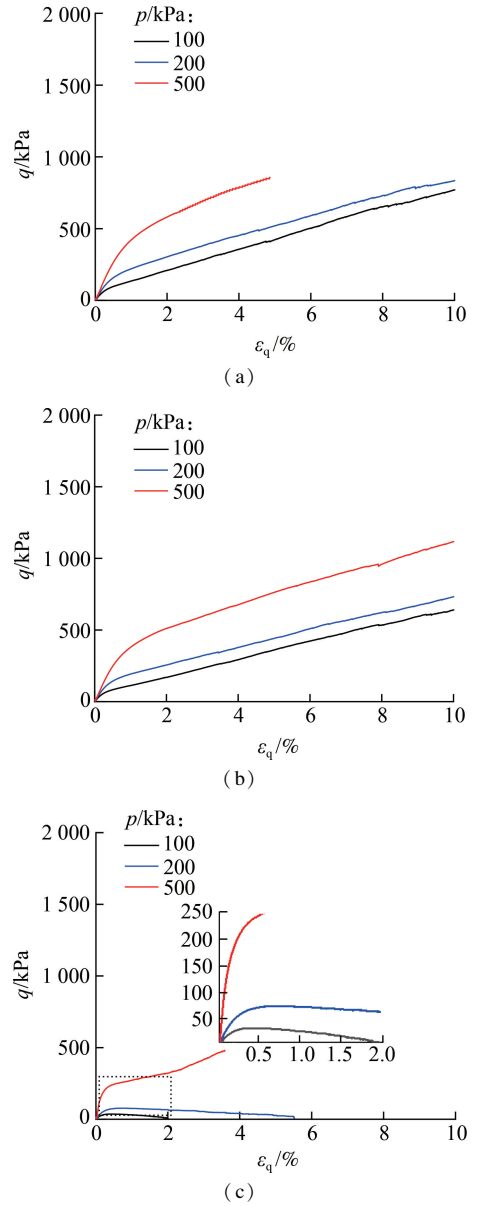

Fig. 7 q vs. ε_q of medium-dense specimens under undrained conditions. (a) $b = 0$; (b) $b = 0.5$; (c) $b = 1.0$

tutive models for granular materials[34]. A deviatoric fabric tensor has two nontrivial invariants, i.e., norm F and direction $\boldsymbol{n}_F$ of $\boldsymbol{F}$. The norm of the fabric F, which represents the degree of the fabric anisotropy, can be calculated as follows:

$$F = \sqrt{\boldsymbol{F} : \boldsymbol{F}} \qquad (5)$$

Hence, $\boldsymbol{F}$ can be expressed as follows:

$$\boldsymbol{F} = F\boldsymbol{n}_F, \quad \boldsymbol{n}_F : \boldsymbol{n}_F = 1$$

$$\mathrm{tr}(\boldsymbol{n}_F) = 0 \qquad (6)$$

In addition, a fabric anisotropy variable A is used to account for the influence of fabric anisotropy and its development on the behavior of the soil sample. To measure the impact of both fabric and external loading direction on soil behavior, Li and Dafalias[25] initially proposed this
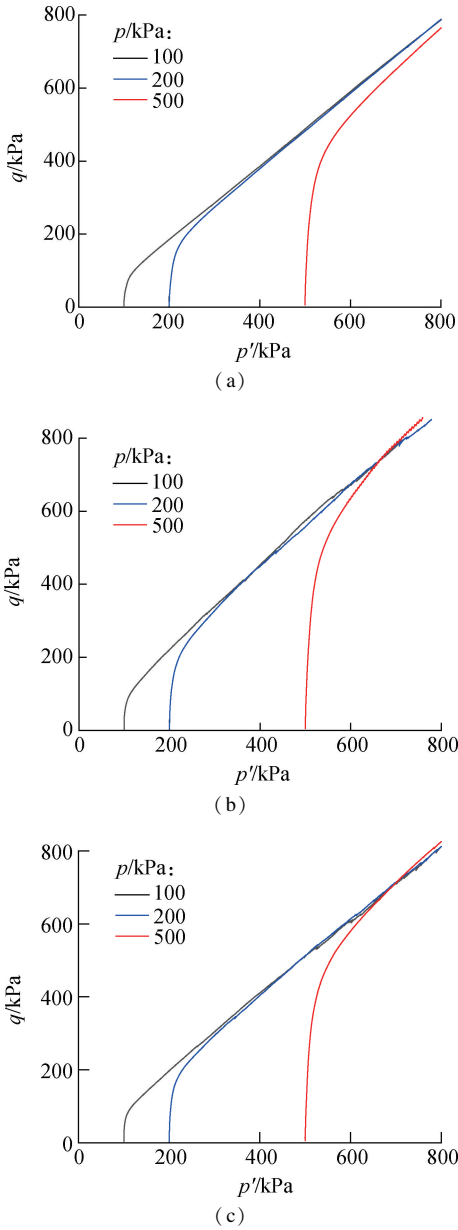
Fig. 8 q vs. p' of medium-dense specimens under undrained conditions. (a) $b=0$; (b) $b=0.5$; (c) $b=1.0$

parameter.

The variable A is calculated as follows:

$$A = \boldsymbol{F} : \boldsymbol{n} = F\boldsymbol{n}_F : \boldsymbol{n} = FN \tag{7}$$

where $N = \boldsymbol{n}_F : \boldsymbol{n}$ is a measure of the orientation between the loading direction $\boldsymbol{n}$ and the fabric direction $\boldsymbol{n}_F$. The loading direction is defined as the direction of deviatoric strain increment and expressed as follows:

$$\boldsymbol{n} = \frac{e_{ij}}{\sqrt{e_{ij} : e_{ij}}} \tag{8}$$

where $e_{ij} = \varepsilon_{ij} - \mathrm{tr}(\varepsilon_{ij})/(3\delta_{ij})$ is the deviatoric strain. According to Eq. (7), the value of N ranges from -1 to 1. When N is equal to 1, the loading direction is codirectional with the fabric direction. Conversely, when N
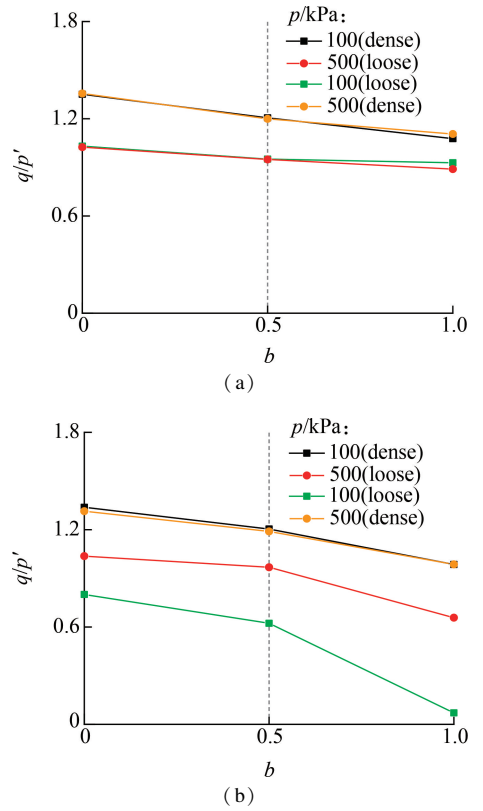

Fig. 9 Summary of the peak stress ratio for both dense and loose specimens considering different b values and confining pressures. (a) Drained; (b) Undrained

Table 3 Comparison between peak values of stress ratio under drained and undrained conditions

Test series	b	Density	$p/$ kPa	q/p' Drained	q/p' Undrained
I	0	Loose	100	1.03	0.80
			200	1.02	1.00
			500	1.02	1.04
		Dense	100	1.35	1.34
			200	1.36	1.34
			500	1.36	1.31
II	0.5	Loose	100	0.95	0.62
			200	0.94	0.97
			500	0.95	0.97
		Dense	100	1.21	1.20
			200	1.20	1.20
			500	1.20	1.19
III	1.0	Loose	100	0.93	0.07
			200	0.90	0.13
			500	0.89	0.66
		Dense	100	1.08	0.99
			200	1.10	0.99
			500	1.11	0.99

is equal to -1, the loading direction is opposite to that of the fiber. When $-1 < N < 1$, a discrepancy exists between loading and fabric directions.

Fig. 10 shows the evolutions of the fabric norm F of dense, medium-dense, and loose specimens under drained conditions. As shown in Fig. 10(a), the b value

tends to have negligible effects on the fabric evolution patterns of specimens under drained conditions. At the early stage of the loading process, specimens under a lower confining pressure of 100 kPa tend to develop a higher degree of fabric anisotropy. At the later stage of the loading process ($\varepsilon_q = 6\%$), the fabric anisotropy of all of the specimens tends to converge into a common value. Similar observations of the fabric evolution patterns can be obtained for medium-dense and dense specimens from Figs. 10(b) and (c), respectively. The comparison of Figs. 10(a), (b), and (c) shows that the confining pressure has a more significant influence on the development of fabric anisotropy of denser specimens.
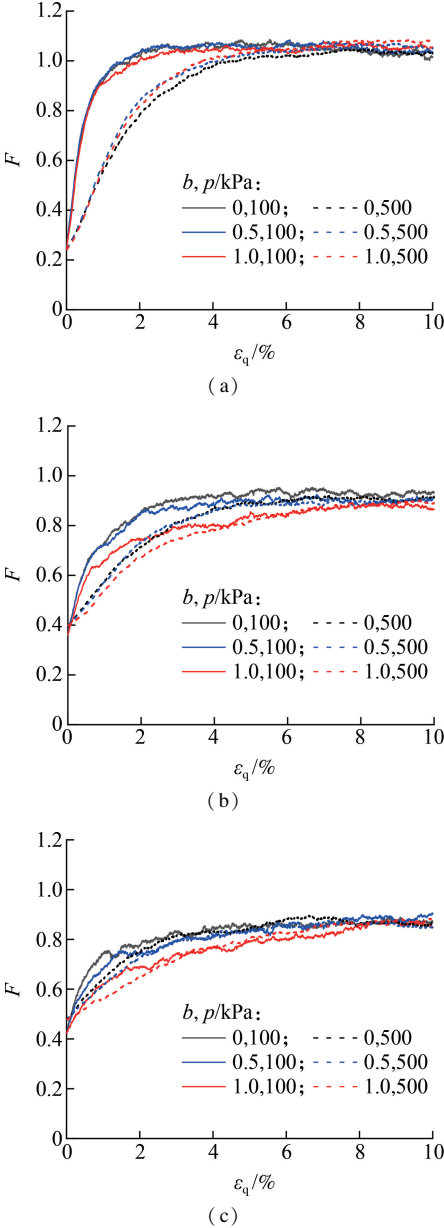

Fig. 10 Evolution of fabric norm F for specimens under drained conditions. (a) Dense; (b) Medium dense; (c) Loose

Fig. 11 shows the fabric evolution patterns of the dense, medium-dense, and loose specimens under undrained conditions. Fig. 11(a) shows that, for the compression cases with $b = 0$ and 0.5, the magnitude of fabric anisotropy continuously increases and then becomes nearly constant. For the extension case with $b = 1.0$, the fabric norm first decreases and then gradually increases as loading proceeds. Fig. 11(a) also shows that, under otherwise identical conditions, the specimens under a lower confining pressure p of 100 kPa tend to exhibit a higher fabric accumulation rate than that under a higher confining pressure p of 500 kPa. Similar observations can be obtained from Figs. 11(b) and (c) for the medium-dense and loose specimens, respectively. The comparison of Figs. 11(a), (b), and (c) shows that denser specimens tend to exhibit a higher fabric anisotropy accumulation rate; therefore, a higher level of fabric anisotropy can be sustained.

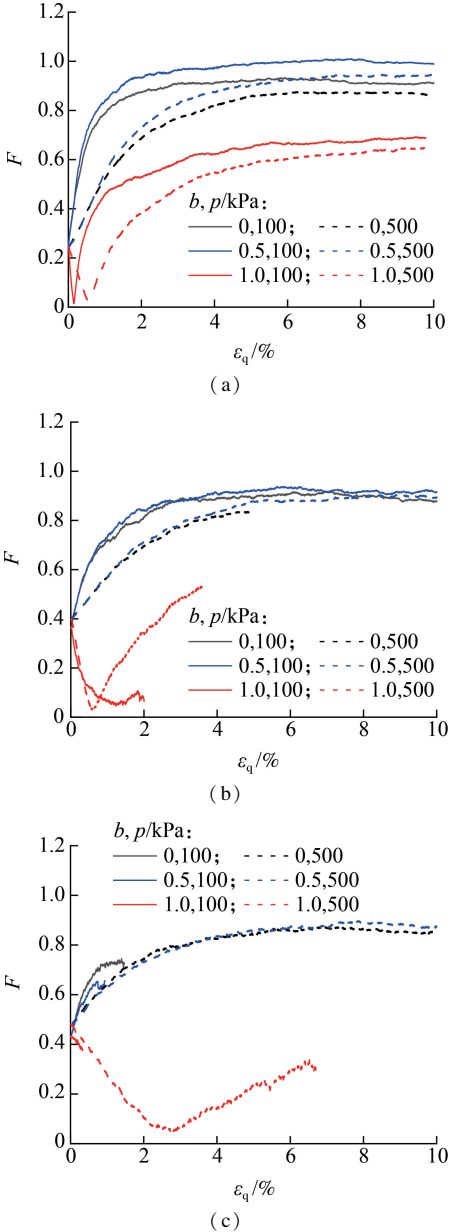Taking the dense specimens as an example, Figs. 12(a)

Fig. 11 Evolution of fabric norm F for specimens under undrained conditions. (a) Dense; (b) Medium dense; (c) Loose

and (b) show the evolution of the parameter N of specimens with $p = 100$ and 500 kPa, respectively. The parameter N quantifies the non-coaxiality between the loading and fabric directions. Fig. 12(a) shows that the loading direction is codirectional with the fabric direction during the entire simulation process for the case with $b = 0$. However, for the cases with $b = 0.5$ and 1.0, a slight discrepancy between loading and fabric directions exists at the early stage of the loading process. As the loading process proceeds, such discrepancies rapidly diminish; therefore, the loading direction becomes codirectional with the fabric direction. The comparison of Figs. 12(a) and (b) shows that the fabric of the specimen under a higher confining pressure tends to take a higher deviatoric strain to become codirectional with the loading direction.
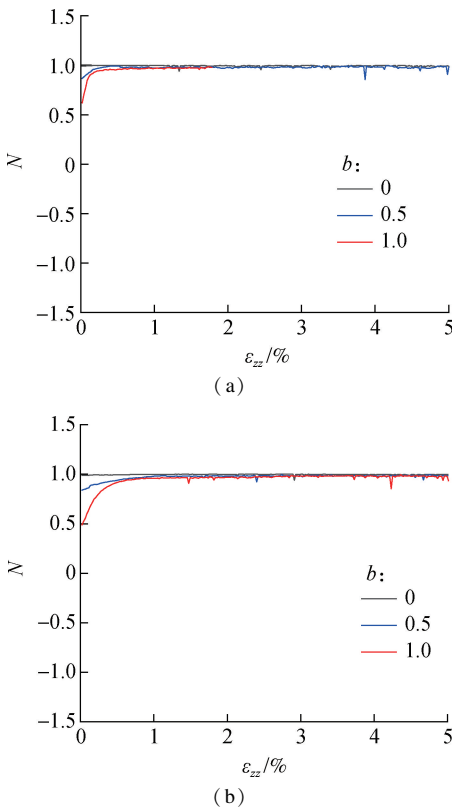

(a)

(b)

Fig. 12 Evolution of the parameter N of dense specimens under drained conditions. (a) $p = 100$ kPa; (b) $p = 500$ kPa

By contrast, Fig. 13 presents the evolution of the parameter N of the dense specimens under undrained conditions. Fig. 13(a) plots the evolution of the parameter N of dense specimens under $p = 100$ kPa. For the case with $b = 0$, $N = 1$ is maintained constant, which means that the loading direction is codirectional with the fabric direction during the entire simulation process. For the case with $b = 0.5$, a slight discrepancy exists ($N < 1$) at the early stage of the loading process. As the loading process proceeds, the fabric evolves gradually toward the loading direction. At $\varepsilon_q = 0.25\%$, N becomes 1 rapidly, indicating the coaxiality between loading and fabric directions. However, for the extension case with $b = 1.0$, the load-

ing direction is opposite to that of the fiber at the early stage of the loading process. As loading continues, the loading direction becomes codirectional ($N = 1$) with the direction of the fabric tensor. Similar observations can be obtained from Fig. 13(b). The comparison of Figs. 13 (a) and (b) shows that the fabric direction of a specimen under lower confining pressure tends to evolve at a faster rate and become codirectional with the loading direction rapidly (at smaller ε_q).
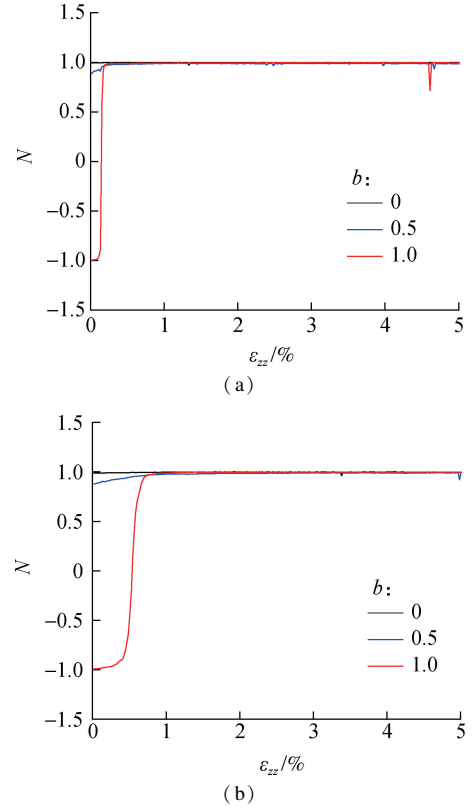

(a)

(b)

Fig. 13 Evolution of the parameter N of dense specimens under undrained conditions. (a) $p = 100$ kPa; (b) $p = 500$ kPa

3 Conclusions

1) Under both drained and undrained conditions, specimens with higher density exhibit higher shear strength and more dilative responses under compression than those under extension. In particular, medium-dense specimens that exhibit strong dilative behavior under compression ($b = 0$ and 0.5) can liquefy under extension ($b = 1.0$). The liquefaction resistance of specimens can be strengthened by increasing confining pressure. Under otherwise identical conditions, the residual stress ratio of specimens under drained and undrained conditions tends to converge.

2) For all of the loading conditions, the magnitude of fabric F increases when the parameter $N > 0$, whereas the magnitude of F decreases when $N < 0$. Under otherwise identical conditions, specimens exhibit similar evolution patterns of fabric norm under drained and undrained conditions. For all specimens, the magnitude of fabric norm

continuously increases under compression but first decreases and then increases under extension. Under compression, a higher fabric anisotropy level can be sustained for the denser specimens. By contrast, a generally smaller fabric anisotropy is observed for the loose specimens, especially under extension.

3) More pronounced non-coaxiality (smaller N) between the loading direction and the major principal direction of the contact-normal-based fabric tensor is observed under extension than those under compression ($b = 0$) under both drained and undrained conditions. This more severe non-coaxiality leads to a stronger tendency of the internal structure to evolve toward the loading direction and, therefore, contributes to weaker resistance to instability and lower shear strength in the extension scenario compared with that in the compression scenario.

References

[1] Barreto D, O'Sullivan C. The influence of inter-particle friction and the intermediate stress ratio on soil response under generalized stress conditions [J]. *Granular Matter*, 2012, **14**: 505 − 521. DOI: 10. 1007/s10035-012-0354-z.

[2] Ochiai H, Lade P V. Three-dimensional behavior of sand with anisotropic fabric [J]. *Journal of Geotechnical Engineering*, 1983, **109**(10): 1313 − 1328. DOI: 10. 1061/(ASCE)0733-9410(1983)109:10(1313).

[3] Oda M. The mechanism of fabric changes during compressional deformation of sand [J]. *Soils and Foundations*, 1972, **12**(2): 1 − 18. DOI: 10. 3208/sandf1972. 12. 1.

[4] Wang Q, Lade P V. Shear banding in true triaxial tests and its effect on failure in sand [J]. *Journal of Engineering Mechanics*, 2001, **127**(8): 754 − 761. DOI: 10. 1061/(ASCE)0733-9399(2001)127:8(754).

[5] Liang M, Ping H. True triaxial tests and strength characteristics study on silty sand [C] // *Proceedings of the 2017 2nd International Conference on Test, Measurement and Computational Method*. Beijing, China, 2017: 131 − 135.

[6] Lade P V, Abelev A V. Effects of cross anisotropy on three-dimensional behavior of sand. Ⅱ: Volume change behavior and failure [J]. *Journal of Engineering Mechanics*, 2003, **129**(2): 167 − 174. DOI: 10. 1061/(ASCE)0733-9399(2003)129:2(167).

[7] Sazzad M M, Suzuki K. Density dependent macro-micro behavior of granular materials in general triaxial loading for varying intermediate principal stress using DEM [J]. *Granular Matter*, 2013, **15**: 583 − 593. DOI: 10. 1007/s10035-013-0422-z.

[8] Huang X, Hanley K J, O'Sullivan C, et al. DEM analysis of the influence of the intermediate stress ratio on the critical-state behavior of granular materials [J]. *Granular Matter*, 2014, **16**: 641 − 655. DOI: 10. 1007/s10035-014-0520-6.

[9] Anandarajah A. Critical state of granular materials based on the sliding-rolling theory [J]. *Journal of Geotechnical and Geoenvironmental Engineering*, 2008, **134**(1): 125

− 135. DOI: 10. 1061/(ASCE)1090-0241(2008)134:1(125).

[10] Tatsuoka F, Sakamoto M, Kawamura T, et al. Strength and deformation characteristics of sand in plane strain compression at extremely low pressures [J]. *Soils and Foundations*, 1986, **26**(1): 65 − 84. DOI: 10. 3208/sandf1972. 26. 65.

[11] Ng T T. Macro-and micro-behaviors of granular materials under different sample preparation methods and stress paths [J]. *International Journal of Solids and Structures*, 2004, **41**(21): 5871 − 5884. DOI: 10. 1016/j. ijsolstr. 2004. 05. 050.

[12] Lade P V, Nam J, Hong W P. Shear banding and cross-anisotropic behavior observed in laboratory sand tests with stress rotation [J]. *Canadian Geotechnical Journal*, 2008, **45**(1): 74 − 84. DOI: 10. 1139/T07-058.

[13] Shi W C, Zhu J G, Chiu C F, et al. Strength and deformation behavior of coarse-grained soil by true triaxial tests [J]. *Journal of Central South University of Technology*, 2010, **17**(5): 1095 − 1102. DOI: 10. 1007/s11771-010-0602-5.

[14] Sivathayalan S, Logeswaran P. Experimental assessment of the response of sands under shear-volume coupled deformation [J]. *Canadian Geotechnical Journal*, 2008, **45**(9): 1310 − 1323. DOI: 10. 1139/T08-057.

[15] Xiao Y, Sun Y, Liu H, et al. Critical state behaviors of a coarse granular soil under generalized stress conditions [J]. *Granular Matter*, 2016, **18**: 1 − 13. DOI: 10. 1007/s10035-016-0623-3.

[16] Abelev A V, Lade P V. Characterization of failure in cross-anisotropic soils [J]. *Journal of Engineering Mechanics*, 2004, **130**(5): 599 − 606. DOI: 10. 1061/(ASCE)0733-9399(2004)130:5(599).

[17] Lade P V. Elasto-plastic stress-strain theory for cohesionless soil with curved yield surfaces [J]. *International Journal of Solids and Structures*, 1977, **13**(11): 1019 − 1035. DOI: 10. 1016/0020-7683(77)90073-7.

[18] Yoshimine M, Ishihara K, Vargas W. Effects of principal stress direction and intermediate principal stress on undrained shear behavior of sand [J]. *Soils and Foundations*, 1998, **38**(3): 179 − 188. DOI: 10. 3208/sandf. 38. 3_179

[19] Yamada Y, Ishihara K. Undrained deformation characteristics of loose sand under three-dimensional stress conditions [J]. *Soils and Foundations*, 1981, **21**(1): 97 − 107. DOI: 10. 3208/sandf1972. 21. 97.

[20] Liu W, Gao Y. Discrete element modeling of migration and evolution rules of coarse aggregates in static compaction [J]. *Journal of Southeast University (English Edition)*, 2016, **32**: 85 − 92. DOI: 10. 3969/j. issn. 1003-7985. 2016. 01. 015.

[21] Xie Y H, Yang Z X, Barreto D, et al. The influence of particle geometry and the intermediate stress ratio on the shear behavior of granular materials [J]. *Granular Matter*, 2017, **19**: 1 − 13. DOI: 10. 1007/s10035-017-0723-8.

[22] Foroutan T, Mirghasemi A A. CFD-DEM model to assess stress-induced anisotropy in undrained granular material [J]. *Computers and Geotechnics*, 2020, **119**: 103318. DOI: 10. 1016/j. compgeo. 2019. 103318.

[23] Foroutan T, Mirghasemi A A. Use of CFD-DEM to evaluate the effect of intermediate stress ratio on the undrained behaviour of granular materials [J]. *Advanced Powder Technology*, 2022, **33**(3): 103507. DOI: 10. 1016/j. apt. 2021. 11. 015.

[24] Lashkari A, Latifi M. A non-coaxial constitutive model for sand deformation under rotation of principal stress axes [J]. *International Journal for Numerical and Analytical Methods in Geomechanics*, 2008, **32**(9): 1051 – 1086. DOI: 10. 1002/nag. 659.

[25] Li X S, Dafalias Y F. Anisotropic critical state theory: Role of fabric [J]. *Journal of Engineering Mechanics*, 2012, **138**(3): 263 – 275. DOI: 10. 1061/(ASCE)EM. 1943-7889. 0000324.

[26] Yang Z, Liao D, Xu T. A hypoplastic model for granular soils incorporating anisotropic critical state theory [J]. *International Journal for Numerical and Analytical Methods in Geomechanics*, 2020, **44**(6): 723 – 748. DOI: 10. 1002/nag. 3025.

[27] Itasca Consulting Group, Inc. PFC manual, version 5. 0 [EB/OL]. (2019-06-18) [2024-05-10]. http://itascacacg. com/software/downloads/pfc-5-00-update.

[28] Cundall P A. A discrete numerical model for granular assemblies [J]. *Geotechnique*, 1979, **29**: 47 – 65. DOI: 10. 1680/geot. 1979. 29. 1. 47.

[29] Jiang M J, Konrad J M, Leroueil S. An efficient technique for generating homogeneous specimens for DEM studies [J]. *Computers and Geotechnics*, 2003, **30**(7): 579 – 597. DOI: 10. 1016/S0266-352X(03)00064-8.

[30] Li X, Yu H S, Li X S. A virtual experiment technique on the elementary behavior of granular materials with discrete element method [J]. *International Journal for Numerical and Analytical Methods in Geomechanics*, 2013, **37**(1): 75 – 96. DOI: 10. 1002/nag. 1093.

[31] Wu Q, Yang Z. Unified discrete-element approach applying arbitrary undrained loading paths in element testing for granular soils [J]. *International Journal for Numerical and Analytical Methods in Geomechanics*, 2023, **47**(1): 3 – 22. DOI: 10. 1002/nag. 3458.

[32] Wu Q, Yang Z. Novel undrained servomechanism in discrete-element modeling and its application in multidirectional cyclic shearing simulations [J]. *Journal of Engineering Mechanics*, 2021, **147**(3): 04020155. DOI: 10. 1061/(ASCE)EM. 1943-7889. 0001896.

[33] Zhao X L. Analysis of granular assembly deformation using discrete element method [J]. *Journal of Southeast University* (*English Edition*), 2010, **26**(4): 608 – 613. DOI: 10. 3969/j. issn. 1003-7985. 2010. 04. 022.

[34] Kanatani K I. Distribution of directional data and fabric tensors [J]. *International Journal of Engineering Science*, 1984, **22**(2): 149 – 164. DOI: 10. 1016/0020-7225(84)90090-9.

排水和不排水条件下砂土真三轴力学行为离散元分析

Seyedeh Fateme Faraji[1]   吴祁新[2]   郑俊杰[1]

(¹ 华中科技大学土木与水利工程学院, 武汉 430074)
(² 武汉大学土木建筑工程学院, 武汉 430072)

摘要:提出了一种离散元伺服机制,能够同时并独立地控制 6 个应力和应变分量的演化,避免应力集中现象. 在真三轴试验中,对排水和不排水压缩剪切条件下横观各向同性砂土的力学响应进行离散元模拟. 模拟过程中,通过基于颗粒间接触法向的组构张量,量化颗粒试件的承力结构演化规律. 结果表明,无论是在排水还是不排水压缩剪切条件下,相较于压缩加载,砂土试件在拉伸时的加载方向与组构主方向上均呈现出更为显著的非共轴性. 试件在拉伸条件下表现出更强的向加载方向演化的趋势,导致承力结构出现更大的扰动. 相较于拉伸条件,横观各向同性试件在排水压缩剪切条件下表现出更高的剪切强度和剪胀性,在不排水压缩剪切条件下则表现出更高的抗液化强度.

关键词:颗粒材料;真三轴试验;离散元方法;组构演化

中图分类号:TU431